

Article

Multi-Timescale Lookup Table Based Maximum Power Point Tracking of an Inverse-Pendulum Wave Energy Converter: Power Assessments and Sensitivity Study

Xuhui Yue ^{1,2,*} , Jintao Zhang ^{1,2}, Feifeng Meng ^{1,2}, Jiaying Liu ^{1,2}, Qijuan Chen ³ and Dazhou Geng ⁴

¹ PowerChina HuaDong Engineering Corporation Limited, Hangzhou 311122, China; zhang_jt@hdec.com (J.Z.); meng_ff@hdec.com (F.M.); liu_jy5@hdec.com (J.L.)

² Hangzhou Huachen Electric Power Control Corporation Limited, Hangzhou 311122, China

³ Key Laboratory of Transients in Hydraulic Machinery, Ministry of Education, Wuhan University, Wuhan 430072, China; qjchen@whu.edu.cn

⁴ China Renewable Energy Engineering Institute, Beijing 100120, China; gengdz@creei.cn

* Correspondence: yue_xh@hdec.com; Tel.: +86-0571-56623055

Abstract: A novel, inverse-pendulum wave energy converter (NIPWEC) is a device that can achieve natural period control via a mass-position-adjusting mechanism and a moveable internal mass. Although the energy capture capacity of a NIPWEC has already been proven, it is still meaningful to research how to effectively control the NIPWEC in real time for maximum wave energy absorption in irregular waves. This paper proposes a multi-timescale lookup table based maximum power point tracking (MLTB MPPT) strategy for the NIPWEC. The MLTB MPPT strategy was implemented to achieve a theoretical “optimal phase” and “optimal amplitude” by adjusting both the position of the internal mass and linear power take-off (PTO) damping. It consists of two core parts, i.e., internal mass position adjustment based on a 1D resonance position table and PTO damping tuning based on a 2D optimal PTO damping table. Furthermore, power assessments and sensitivity study were conducted for eight irregular-wave sea states with diverse wave spectra. The results show that energy period resonance and the lookup table based PTO damping tuning have the highest possibility of obtaining the maximum mean time-averaged absorbed power. Additionally, both of them are robust to parameter variations. In the next step, the tracking performance of the MLTB MPPT strategy in terms of changing sea states will be studied in-depth.

Keywords: wave energy converter; maximum power point tracking; multi-timescale lookup table; internal-mass position adjustment; PTO damping tuning; power assessments; sensitivity study



Citation: Yue, X.; Zhang, J.; Meng, F.; Liu, J.; Chen, Q.; Geng, D.

Multi-Timescale Lookup Table Based Maximum Power Point Tracking of an Inverse-Pendulum Wave Energy Converter: Power Assessments and Sensitivity Study. *Energies* **2023**, *16*, 6195. <https://doi.org/10.3390/en16176195>

Academic Editors: Eugen Rusu, Vincenzo Franzitta, Daniele Milone, Domenico Curto and Andrea Guercio

Received: 13 June 2023

Revised: 16 August 2023

Accepted: 24 August 2023

Published: 25 August 2023



Copyright: © 2023 by the authors. Licensee MDPI, Basel, Switzerland. This article is an open access article distributed under the terms and conditions of the Creative Commons Attribution (CC BY) license (<https://creativecommons.org/licenses/by/4.0/>).

1. Introduction

Wave energy is a carbon-free renewable resource that possesses the advantages of a high energy density and has outstanding availability and better predictability than wind or solar energy [1]. Besides, the global wave power is about 29,500 TWh/year, according to the estimation from Ocean Energy Systems [2]. If wave energy is fully utilized, the demand for global electricity consumption can be sufficiently satisfied. The data given by the International Energy Agency show that the global electricity consumption in 2019 reached 22,848 TWh [3]. Therefore, wave energy has enormous development potential.

However, there still exist several technical and non-technical challenges for wave energy utilization (WEU) [1,4]. The wave-by-wave, hour-by-hour, and site-by-site variations of the level of wave power represent one of the main obstacles restricting technological convergence and maturity. Therefore, many researchers focus on how to improve the performance of wave energy converters (WECs), especially wave conversion efficiency, under complex sea states [5].

WEC operation control has always been deemed a research hot spot since a successful control method can significantly enhance the wave conversion efficiency of an existing WEC

with low additional investment [1]. To date, plenty of control methods have been proposed based on different actuators and control algorithms, wherein the phase control methods (PCMs), natural period control methods (NPCMs), and maximum power point tracking (MPPT) are related to the research content of this paper. Hence, the aforementioned three control methods are introduced respectively.

PCMs, e.g., latching control (LC) and declutching control (DeC), were first presented between the end of the 1970s and the beginning of this century. PCMs are usually based on PTO force tuning, which can compulsively synchronize WEC movement with the variations in wave excitation force to achieve an “optimal phase”. The theoretical basis of PCMs was summarized by Falnes [6] as a universal theory on ocean waves and oscillating systems. Although the theory is linear, it qualitatively points out the core idea of most control methods, not only PCMs. Herein, the core idea means that the maximum absorbed power will appear when both “optimal phase” and “optimal amplitude” are achieved. “Optimal phase” denotes a resonant state where the WEC velocity and wave excitation force are in phase. Meanwhile, “optimal amplitude” refers to damping matching; e.g., the linear damping of a power take-off (PTO) should be equal to radiation damping in regular waves. Nowadays, LC or DeC, with or without the knowledge of future excitation force, still attracts many researchers [7,8].

NPCMs are another solution for achieving “optimal phase”. They alter the natural period/frequency of a WEC to be identical to the period/frequency of an incident wave. Three ways can be used to realize natural period control. The first is inertia adjustment [9,10], the second can be called stiffness adjustment (SA) [11–16], and the third is known as surface control [17]. SA is the most common NPCM. It refers to adjusting the inherent stiffness term in a WEC. Marei et al. [11] changed compressed gas stiffness to achieve the resonance of an Archimedes wave swing. Additionally, Chen et al. [12] implemented the SA of a built-in horizontal axis pendulum to achieve resonance. Moreover, Refs. [13–16] pointed out that the hydrostatic restoring stiffness of an oscillating wave surge converter (OWSC), e.g., a solo duck WEC or an inverse-pendulum-type WEC, can be effectively regulated for resonance by using a moveable mass.

When compared to PCMs, NPCMs are mainly based on slow tuning processes. It means that energy capture performance can be effectively improved as long as a WEC adjusts its natural period to the wave characteristic period of an irregular wave within a large duration. In addition, NPCMs do not need to tune PTO force at a wide range, which reduces the control difficulty and improves control reliability. However, NPCMs are only able to realize “optimal phase”. If “optimal amplitude” is required, PTO force tuning should be inevitably adopted. Therefore, how to comprehensively design and utilize two control mechanisms to achieve both “optimal phase” and “optimal amplitude” could become an issue worthy of in-depth research when applying NPCMs.

MPPT is a real-time search technology for the maximum power points of clean energy power, such as wind power, photovoltaics, thermoelectricity [18], etc. In 2009, Amon et al. [19] first introduced the concept of MPPT to WEU, conducting a perturbation and observation (P&O) algorithm on the duty cycle of a Buck circuit as well as the simulated resistance of a three-phase pulse width modulation (PWM) rectifier. Nowadays, the MPPT algorithm family includes a fixed-step P&O [19–22], a variable-step P&O [23,24], a segmental fixed-step P&O [25], a lookup-table-based (LTB) MPPT [26,27], diverse heuristic algorithms [28,29], etc. The fixed-step P&O is the most common algorithm and often serves as a reference for other algorithms. Besides, LTB MPPT is an ordinary but practical algorithm that has been applied to an oscillating water column-type WEC and a floating-pendulum WEC [26,27]. Yue et al. [27] proved that a two-dimensional (2D) LTB MPPT algorithm, which contains an optimal duty cycle table derived from regular wave simulations, is a simple, reliable, and excellent solution for WEC output power enhancement in irregular waves. Refs. [30,31] constructed an emulator for a point absorber WEC (PAWEC) and reviewed the MPPT techniques or hybrid strategies of PAWECs.

This paper focuses on a novel inverse-pendulum wave energy converter (NIPWEC), which can conduct SA via a mass-position-adjusting mechanism (MPAM) and a moveable internal mass. The structural details of a NIPWEC can be seen in Section 2. Similar structures can be seen in Refs. [14–16,32]. Although the energy capture capacity of a NIPWEC has already been proven via simulations in a numerical wave tank, the prototype tests in a physical wave flume and the annual average power assessments of a 1:16 full-scale prototype [14,15] for how to effectively control the NIPWEC in real-time is still a meaningful research topic. The inefficient implementation of a control method can lead to ordinary or even weakened energy capture performance. Hence, this paper researches an implementation strategy for SA and PTO force tuning, aiming to find a suitable control algorithm for NIPWECs for real irregular waves.

Dong et al. [32] proposed a frequency and amplitude control (FAC) strategy to realize the MPPT of a NIPWEC. Herein, frequency control means adjusting the internal mass position according to the peak frequency of a wave spectrum. Meanwhile, amplitude control refers to tuning the PTO force to find the inherent impedance of the NIPWEC, which is approximately calculated by a weighted average method. The premise of FAC is the fast Fourier transformation (FFT) and frequency-domain analysis of the wave excitation moment within the past hundreds of seconds at least. This may lead to the following two issues.

(1) The nonlinear factors, e.g., an endstop moment for the swing amplitude limitation and a sine function hydrostatic restoring moment, are ignored by frequency domain analysis. This may result in the deterioration of MPPT performance when the ideal NIPWEC inherent impedance is applied to PTO force tuning.

(2) The real-time tracking performance may be weakened since both frequency control and amplitude control are implemented every few hundred seconds.

In contrast to Ref. [32], this paper presents a simple and reliable control algorithm, i.e., the multi-timescale lookup table based maximum power point tracking (MLTB MPPT), for NIPWECs. This algorithm is constructed and conducted based on a similar idea that can be found in Ref. [27]. MLTB MPPT consists of LTB internal-mass position adjustment and LTB PTO damping tuning, which are obtained via time domain analysis with consideration given to the above nonlinear factors. Additionally, MLTB MPPT is capable of tuning the PTO force wave by wave, which can reinforce its real-time tracking performance. Detailed descriptions of MLTB MPPT are illustrated in Section 2. Furthermore, the power assessments and sensitivity study of MLTB MPPT are comprehensively investigated.

The rest of this paper is organized as follows. First, the structure and implementation procedure of MLTB MPPT is elaborated in Section 2. Next, a NIPWEC dynamic model is described in Section 3. Then, the parameter settings for the time domain simulations are displayed in Section 4. Afterwards, the maximum-power-point (MPP) analysis in regular waves, as well as the power assessments and sensitivity study for MLTB MPPT in irregular waves, is discussed in Section 5. Last, the conclusions, along with future work discussion, are revealed in the Section 6.

2. Methodology: MPPT

2.1. Three MPPT Implementation Methods for a NIPWEC

We focus on a NIPWEC with a mechanical power take-off. As shown in Figure 1, the NIPWEC is constrained on a fixed supporting shaft and swings along it driven by ocean waves. Next, a speed-increase mechanism accelerates the inverse-pendulum swing and converts it into the fast bidirectional rotation of a permanent magnet synchronous generator (PMSG). Then, the PMSG generates continuous but unstable three-phase alternating-current (AC) electricity. Afterwards, a three-phase PWM rectifier transforms the AC electricity into direct current (DC) and regulates the PTO force via the vector control of a PMSG. Last, the DC bus smooths DC voltage and balances power generation and consumption via an energy storage unit and diverse electric loads.

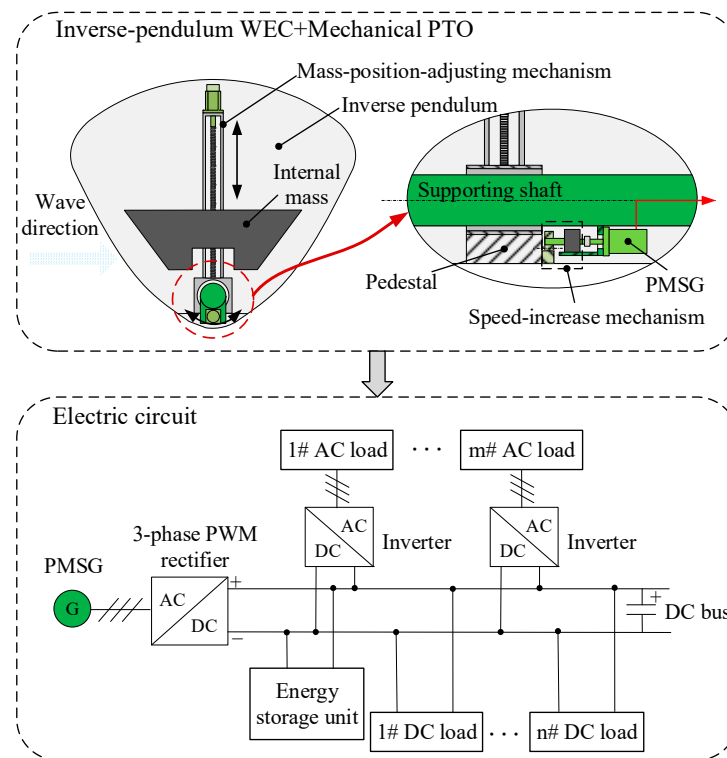


Figure 1. Mechanical structure and electrical topology of the NIPWEC with a DC bus.

The NIPWEC can automatically tune its natural period within a wide range by adjusting the vertical position of an internal mass, according to the changing characteristic period of irregular waves. Herein, the mass position-adjusting mechanism (MPAM) with a screw and a motor is adopted. The motor drives the screw to rotate forward/reverse in order to realize the up/down movement of the internal mass. Therefore, the NIPWEC is able to generate electricity at the resonant state for a long time, which leads to the effective improvement of the energy capture/generating capacity.

Falnes [6] pointed out that the single DoF motion in ocean waves can be assumed to be a forced linear oscillation system. Under this assumption, the maximum absorbed power can be obtained under the “optimal phase” condition, which means that the oscillation velocity and excitation force are in phase. However, Falnes’ theory relies on a frequency domain model and ignores the influence of nonlinear factors, e.g., an endstop moment for the swing amplitude limitation and a sine function hydrostatic restoring moment [33]. The two nonlinear factors are able to significantly affect the magnitude of the absorbed power under the “resonance” condition. This means that due to the existence of nonlinear factors, the optimal PTO damping R_{PTOmax} is not exactly equal to the radiation damping $R_{55}(\omega_r)$ at resonance wave frequency ω_r . In addition, the actual ocean waves are irregular waves, for which the wave heights and wave periods change all the time. Therefore, it is meaningful to search for a simple and reliable MPPT algorithm based on a time domain model.

The basic goal of an MPPT algorithm is to achieve “optimal phase”, i.e., resonance, and “optimal amplitude”, i.e., optimal PTO damping, against the maximum absorbed power. For a NIPWEC, the above goal can be theoretically achieved via the following three implementation methods.

Method 1 (M1): adjust the internal mass position X to achieve “optimal phase” and tune PTO damping R_{PTO} to achieve “optimal amplitude”. Herein, $X = l_M(t) - l_{M0}$, where l_{M0} means the lower bound for $l_M(t)$, and $l_M(t)$ signifies the distance between the rotation center R and the adjustable internal mass center M . The PTO moment M_{PTO} for M1 can be given by

$$M_{PTO} = -R_{PTO}\dot{\theta} \quad (1)$$

Method 2 (M2): adjust the PTO stiffness K_{PTO} to achieve “optimal phase” and tune R_{PTO} to achieve “optimal amplitude”. M_{PTO} for M2 is

$$M_{PTO} = -R_{PTO}\dot{\theta} - K_{PTO}\theta \quad (2)$$

Method 3 (M3): M3 is similar to M2; the only difference from M2 is that the sine function hydrostatic restoring moment is considered when adjusting K_{PTO} . M_{PTO} for M3 is

$$M_{PTO} = -R_{PTO}\dot{\theta} - K_{PTO}\sin\theta \quad (3)$$

2.2. MLTB MPPT

2.2.1. Overall Structure

Section 2.1 has already pointed out that a feasible MPPT implementation method is M1, i.e., simultaneously adjusting X and R_{PTO} . The details of the real-time MPPT technology in irregular waves are discussed in this section. Herein, we propose a simple and reliable MLTB MPPT (see Figure 2), which is embedded in the wave power controller of a NIPWEC. MLTB MPPT contains two core parts, i.e., LTB internal-mass position adjustment and LTB PTO damping tuning.

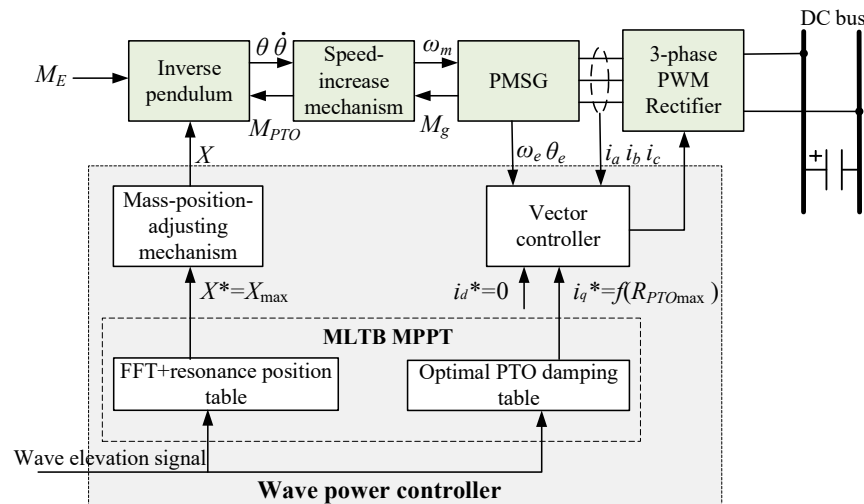


Figure 2. Schematic diagram of the control structure for MLTB MPPT.

In terms of LTB internal-mass position adjustment, the precise adjustment of X can be realized via the MPAM with a screw and a controllable motor, e.g., a servo or stepper motor. The controllable motor drives the screw to rotate and to move the internal mass to a reference position X^* , which can be given by querying the resonance position table according to the estimated characteristic period of a real-time wave spectrum. The real-time wave spectrum can be obtained through the FFT for the in situ wave elevation signal (WES) within the past hundreds of seconds. Herein, WES can be dependably achieved via the in situ wave-measuring buoy. Additionally, WEC motion can be utilized to identify wave excitation force/moment [14,34,35]. Thereby, WES could be theoretically estimated via the identified wave excitation force/moment and the corresponding transfer function. However, few papers focus on the relevant issue.

For LTB PTO damping tuning, the accurate tuning of R_{PTO} can be achieved by applying vector control to the PMSG using a three-phase PWM rectifier. The vector controller adopts a 0-d-axis-current control mode. Structurally, it only contains a current loop with the reference d-axis current $i_d^* = 0$. Meanwhile, the reference q-axis current i_q^* is given by a function of R_{PTOmax} , which can be retrieved from the optimal PTO damping table according to the period and height of the last single wave or the statistical period and height of a previous multiple-wave group.

Herein, “multi-timescale” is reflected in two aspects. First, the required historical WES for the LTB internal-mass position adjustment and the LTB PTO damping tuning is different in terms of the signal length. The former needs a several-hundred-second WES to accurately calculate the characteristic period of a real-time wave spectrum, whereas the latter only needs the WES within the duration of a single wave or multiple waves. Second, there also exists a distinction between the implementation time intervals for the LTB internal-mass position adjustment and the LTB PTO damping tuning. Internal mass position can be adjusted at intervals of the kilo-second level since the obvious change of a real-time wave spectrum only occurs hourly [1,36]. Meanwhile, PTO damping should be tuned wave-by-wave or “waves-by-waves”, which means that the implementation time intervals of PTO damping tuning lie at the second or minute level.

Furthermore, “look-up table” refers to the two key tables, i.e., the resonance position table and the optimal PTO damping table, derived from the MPP analysis for regular waves. Both of them are essential for guiding the MPPT in terms of regular waves.

When compared to other MPPT algorithms, MLTB MPPT has the following two features.

(1) MLTB MPPT has high reliability. It can effectively avoid search blindness, as the two look-up tables offer a meaningful reference for improving search accuracy.

(2) The principle of MLTB MPPT is simple. Complex wave prediction is unnecessary. Moreover, the two look-up tables can be easily obtained through a batch of regular wave simulations without regard given to irregular waves.

2.2.2. LTB Internal-Mass Position Adjustment

The internal mass position should be adjusted adaptively, along with the changeable real-time wave spectrum, to make sure that the NIPWEC can generate electricity at the resonant state most of the time. The core of the internal-mass position adjustment locates and keeps the natural period of the NIPWEC consistent with the characteristic period T_c . Therefore, the adjusting process can be conducted as follows:

- S1. Preset adjusting cycle, ΔT_m .
- S2. Set sequence number, $n_t = 0$.
- S3. Obtain the WES and save it.
- S4. Determine whether running time $\geq n_t \Delta T_m$. If the inequality is satisfied, go to S5. Otherwise, keep running S3.
- S5. Implement FFT and filtering on the historical WES within the duration of dT_m after the instant of $n_t \Delta T_m$ to obtain the real-time wave spectrum.
- S6. Calculate the T_c of the real-time wave spectrum.
- S7. Search the resonance position table and find out the resonance position X_{\max} corresponding to T_c . If T_c cannot be found in the resonance position table, an interpolation should be employed.
- S8. Set $X^* = X_{\max}$ and input X^* into the MPAM.
- S9. Move the internal mass to the given position X^* via an MPAM and keep the position.
- S10. Determine whether the program needs to be stopped. If yes, terminate the program. Otherwise, $n_t = n_t + 1$ and return to S3.

2.2.3. LTB PTO Damping Tuning

If we assume that each single wave in an irregular wave sequence can be seen as a regular wave within the duration of a wave period, the corresponding $R_{PTO\max}$ given by an optimal PTO damping table can be applied wave-by-wave, i.e., every other wave period, to approach the real-time “optimal amplitude” condition. Although a single wave is not completely sinusoidal, the aforementioned assumption is essential and suitable for practical engineering. Furthermore, a 2D LTB MPPT algorithm with the same assumption has already been proposed and verified by Ref. [27]. The only difference between the 2D LTB MPPT and the LTB PTO damping tuning here is that the control variable of the 2D LTB MPPT refers to the duty cycle of a buck-boost converter.

Similar to the 2D LTB MPPT, LTB PTO damping tuning can be implemented wave-by-wave or waves-by-waves, i.e., at intervals of multiple wave periods. The first implementation strategy is named single-wave-period tuning (SWPT), whereas the second can be called multiple-wave-period tuning (MWPT). If frequent adjustment is not wanted, MWPT could be an alternative with comparable performance. Moreover, since there is not much difference in the periods/heights of the two adjacent single waves as well as the statistical periods/heights of the two adjacent multiple-wave groups, the corresponding R_{PTOmax} of the last single wave or multiple-wave group is utilized for the present one here in order to avoid complex wave prediction.

The procedure of SWPT is described below.

- S1. Preset the single wave order number to $n = -1$.
- S2. Obtain the WES and save it.
- S3. Determine whether it reaches the $n+1$ -th up-crossing zero point $Z_{up,n+1}$. If yes, $n = n + 1$ and go to S4. Otherwise, return to S2.
- S4. Determine whether $n > 0$. If yes, go to S5. Otherwise, return to S2.
- S5. Calculate the height H_n and period T_n of the n -th single wave.
- S6. Search the optimal PTO damping table and find out the R_{PTOmax} corresponding to (H_n, T_n) . If (H_n, T_n) cannot be found exactly in the optimal PTO damping table, an interpolation should be employed.
- S7. Set $i_q^* = f(R_{PTOmax})$ and input it into the vector controller. Since the 0-d-axis-current control mode is adopted, $f(R_{PTOmax})$ can be expressed as

$$f(R_{PTOmax}) = -\frac{R_{PTOmax}\omega_m}{1.5n_p\phi_f k_g^2} \quad (4)$$

where ω_m is the PMSG angular velocity, n_p is the number of pole pairs, ϕ_f is the rotor flux, and k_g is the acceleration ratio of a speed increase mechanism.

- S8. Tune R_{PTO} to R_{PTOmax} via the PMSG vector control and keep R_{PTO} .
- S9. Determine whether the program needs to be stopped. If yes, terminate the program. Otherwise, return to S2.

In addition, the procedure of MWPT is as follows:

- S1. Preset the single wave order number to $n = -1$.
- S2. Define the number of single waves k_w ($k_w > 1$).
- S3. Obtain the WES and save it.
- S4. Determine whether it reaches the $n+1$ -th up-crossing zero point $Z_{up,n+1}$. If yes, $n = n + 1$ and go to S5. Otherwise, return to S3.
- S5. Determine whether $n > 0$. If yes, go to S6. Otherwise, return to S3.
- S6. Calculate the height H_n and period T_n of the n -th single wave.
- S7. Determine whether n is the multiple of k_w . If yes, go to S8. Otherwise, return to S3.
- S8. Calculate the statistical height H_{k_w} and statistical period T_{k_w} of the multiple-wave group containing the last k_w single waves. Herein, the mean wave height and period for the first one-third of the single waves of the multiple-wave group, which is rearranged in descending order of k_w wave heights, is chosen as H_{k_w} and T_{k_w} .
- S9. Search the optimal PTO damping table and find the R_{PTOmax} corresponding to (H_{k_w}, T_{k_w}) . If (H_{k_w}, T_{k_w}) cannot be exactly found in the optimal PTO damping table, an interpolation should be employed.
- S10. Set $i_q^* = f(R_{PTOmax})$ and input it into the vector controller.
- S11. Tune R_{PTO} to R_{PTOmax} via the PMSG vector control and keep R_{PTO} .
- S12. Determine whether the program needs to be stopped. If yes, terminate the program. Otherwise, return to S3.

2.2.4. The Two Other PTO Damping Tuning Algorithms

The two other PTO damping tuning algorithms were also researched for a comparison with the LTB PTO damping tuning. The first one is a fixed-step P&O algorithm, and the second is a variable-step P&O algorithm, i.e., the admittance differentiation method (ADM).

The structure of a fixed-step P&O algorithm is shown in Figure 3. Herein, R_{PTO} is perturbed with a fixed-step ΔR_{PTO} in order to search the maximum absorbed power P_{PTO} in real time. The update duration of R_{PTO} is set as ΔT . This means R_{PTO} is automatically updated at time intervals of ΔT . The perturbation direction of R_{PTO} will be flipped once the P_{PTO} value at present is lower than that at the previous moment. Similar algorithms were adopted in Refs. [19–22].

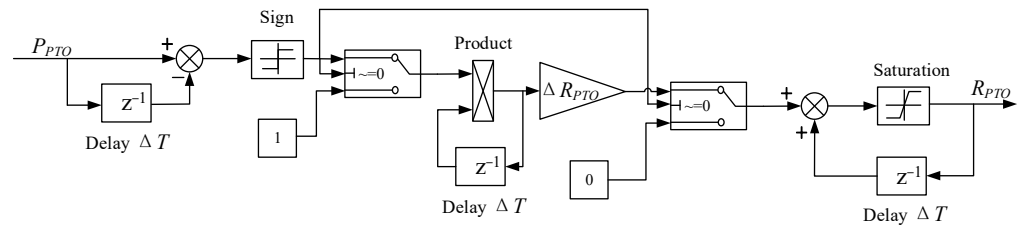


Figure 3. Block diagram of the fixed step P&O algorithm.

ADM is based on the moving-least-square (MLS) power forecast and maximum capture width ratio (CWR) tracking. An analogous algorithm is described in Ref. [24]. The structure of an ADM is displayed in Figure 4. Herein, R_{PTO} is perturbed with a variable step size ΔR_{PTO_ADM} . ΔR_{PTO_ADM} is given by

$$\Delta R_{PTO_ADM} = a \frac{CWR}{R_{PTO_ADM,-1} - R_{PTO_ADM,-2}} = a \frac{(P_{PTO} - P_{PTO_forecast}) / P_{wave}}{R_{PTO_ADM,-1} - R_{PTO_ADM,-2}} \quad (5)$$

where a means the step size coefficient, CWR the capture width ratio, $R_{PTO_ADM,-1}$ or $R_{PTO_ADM,-2}$ the PTO damping at the last moment or the moment before last, $P_{PTO_forecast}$ the absorbed power predicted by a MLS power forecast, and P_{wave} as the input wave power $P_{wave} = J_{ir}b$. J_{ir} is the wave power per unit width for irregular waves, and b is the NIPWEC dimension perpendicular to the wave propagation direction.

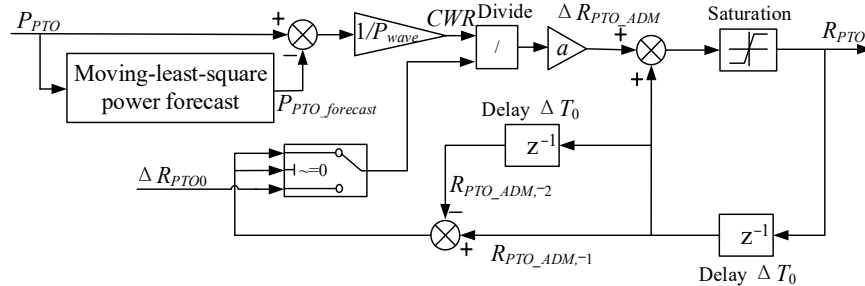


Figure 4. Block diagram of the ADM. Note: $\Delta R_{PTO0} = 50$ Nms; $\Delta T_0 = 0.01$ s.

3. Model: NIPWEC Dynamics

Based on Figure 5, the dynamic model of a NIPWEC can be expressed as the following Cummins' equation [37].

$$(J_{P+M}(I_M(t)) + J_{55\infty})\ddot{\theta}(t) + \int_0^t K(t - \tau)\dot{\theta}(\tau)d\tau + (F_B l_B - G_P l_P - G_M I_M(t)) \sin \theta(t) = M_E + M_{PTO} + M_{end} \quad (6)$$

where J_{P+M} is the total moment of inertia, $J_{55\infty}$ the additional mass at the wave frequency of $+\infty$, θ is the swing angle, $K(t)$ is the impulse response function of $K(\omega)$, F_B is the buoyancy force, G_P is the pendulum-hull gravity force, G_M is the internal-mass gravity force, l_B or l_P is the distance between the rotation center R and the buoyancy center B or the pendulum-hull mass center P, M_E is the wave excitation moment, M_{PTO} is the PTO moment, M_{end} is the endstop moment to prevent θ from exceeding its limits.

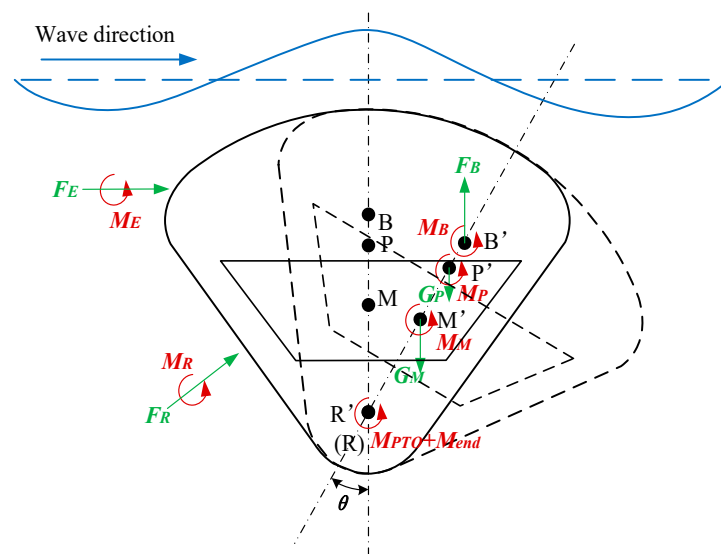


Figure 5. Force analysis of the NIPWEC. Herein, F_E , F_R , G_M , G_P , and F_B mean the wave excitation force, radiation force, internal-mass gravity force, pendulum-hull gravity force, and buoyancy force, respectively, M_E , M_R , M_M , M_P , and M_B are the corresponding moments against R.

J_{P+M} is the function of $l_M(t)$, and can be described by

$$J_{P+M} = J_P + J_{M0} + m_M l_M^2(t) \tag{7}$$

where J_P is the pendulum-hull moment of inertia against R, J_{M0} is the internal mass moment of inertia against M, m_M is the internal-mass mass.

$K(\omega)$ can be represented as

$$K(\omega) = R_{55}(\omega) + j\omega(J_{55}(\omega) - J_{55\infty}) \tag{8}$$

where $R_{55}(\omega)$ and $J_{55}(\omega)$ denote the radiation damping and additional mass against R, respectively.

According to Ref. [38], M_E can be written as

$$M_E(t) = \sum_{j=1}^m f_{e5}(\omega_j) A(\omega_j) \cos(\omega_j t + \theta_{e5}(\omega_j) + 2\pi \text{rand}()) \tag{9}$$

where m is the number of wave frequency elements, ω_j the j -th wave frequency element, f_{e5} and θ_{e5} are the amplitude and phase angle of the excitation-force coefficient, respectively, A is the wave amplitude, and $\text{rand}()$ is a random number in (0,1). The expression of A has already been revealed in Ref. [27]. This expression is based on the random interval division for wave frequency elements in order to avoid reproducing the WES or $M_E(t)$.

M_{PTO} and M_{end} can be given by

$$M_{PTO} = -k_g M_g \tag{10}$$

$$M_{end} = r_{end} F_{end} \tag{11}$$

where M_g is the PMSG moment, and r_{end} is the distance from R to the action point of the endstop force F_{end} . Detailed formulas for M_g and F_{end} can be seen in Ref. [39].

4. Parameter Settings

4.1. NIPWEC

We took the NIPWEC with a width of 5 m and a side area of 20 m² as a research case. The overall appearance and dimensions are illustrated in Figure 6. The detailed design parameters of this NIPWEC are listed in Table 1. In addition, the frequency-domain curves for the hydrodynamic parameters are shown in Figure 7.

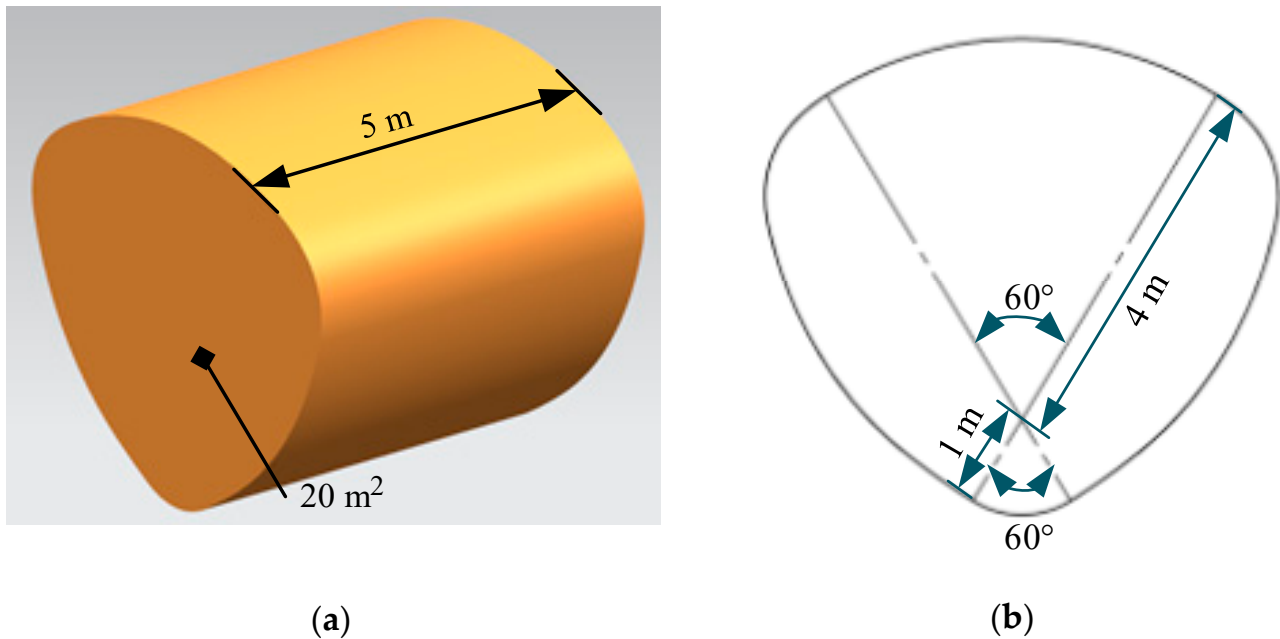


Figure 6. The appearance and dimensions of the researched NIPWEC. (a) A three-dimensional view. (b) The basic dimensions of the side profile.

Table 1. The design parameters of the researched NIPWEC.

Parameter	Value	Unit
J_P	5.138×10^4	[kg·m ²]
J_{M0}	1.025×10^5	[kg·m ²]
m_M	9.306×10^4	[kg]
l_{M0}	0.2	[m]
J_{55°	1.844×10^5	[kg·m ²]
F_B	1.014×10^6	[N]
l_B	1.726	[m]
G_P	1.015×10^5	[N]
l_P	1.12	[m]
G_M	9.129×10^5	[N]
m	300	[-]
Distance between R and the still water level	6	[m]
k_g	120	[-]
n_p	3	[-]
ϕ_f	0.6	[Wb]

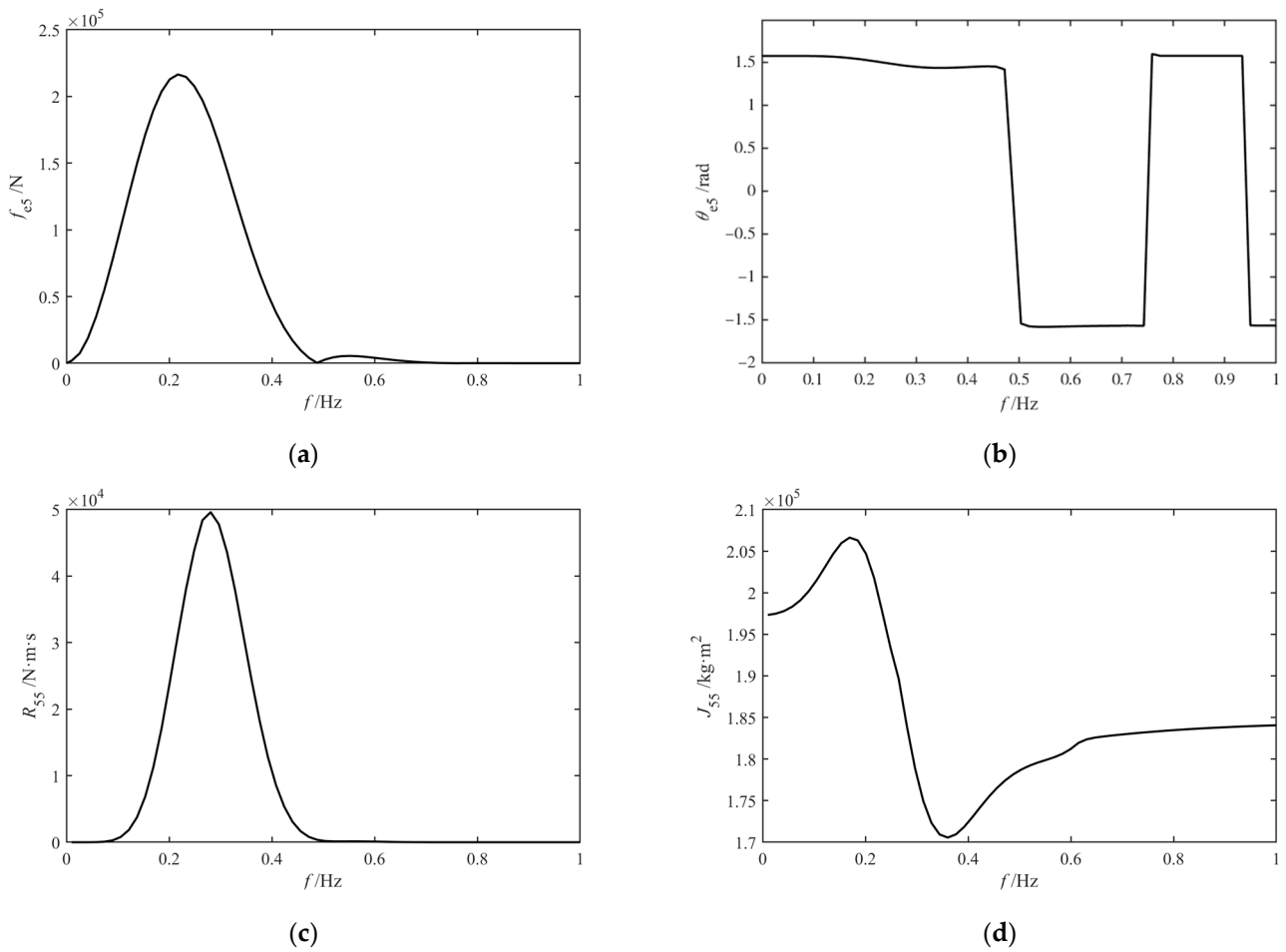


Figure 7. Frequency-domain curves for the hydrodynamic parameters of the researched NIP-WEC. **(a)** Excitation force coefficient amplitude: f_{e5} . **(b)** Excitation-force-coefficient phase angle: θ_{e5} . **(c)** Radiation damping: R_{55} . **(d)** Additional mass: J_{55} .

4.2. Irregular Wave Environments

Irregular wave simulations were implemented in MATLAB/Simulink. In order to study the applicability of MLTB MPPT for diverse irregular waves, the following three common wave spectrums are introduced to simulate irregular wave environments.

(1) JONSWAP spectrum [40]

$$\begin{cases} S_{\omega}(\omega) = \alpha H_s^2 \left(\frac{2\pi}{T_p}\right)^4 \omega^{-5} \exp\left(-\frac{5}{4} \left(\frac{2\pi}{T_p}\right)^4 \omega^{-4}\right) \gamma^a \\ a = \exp\left(-\frac{1}{2\sigma^2} \left(\frac{\omega}{2\pi} T_p - 1\right)^2\right) \end{cases} \quad (12)$$

where H_s and T_p are the significant wave height and the peak period, respectively, γ ($1 < \gamma < 10$) means the peak elevation factor, σ signifies the peak shape parameter, and α is the energy scale parameter that ensures the validity of the following equation:

$$H_s^2 = 16 \int_0^{\infty} S_{\omega}(\omega) d\omega \quad (13)$$

wherein γ is positively correlated with the slenderness of a spectrum peak. When $\gamma = 3.3$, the wave spectrum can also be called a “standard JONSWAP spectrum”. Moreover, σ is given segmentally in the frequency domain. The formula of σ is

$$\sigma = \begin{cases} 0.07, \omega \leq \frac{2\pi}{T_p} \\ 0.09, \omega > \frac{2\pi}{T_p} \end{cases} \quad (14)$$

(2) Pierson-Moskowitz (P-M) spectrum [40]:

$$\begin{cases} S_\omega(\omega) = \frac{1}{4\pi} H_s^2 \left(\frac{2\pi}{T_z}\right)^4 \omega^{-5} \exp\left(-\frac{1}{\pi} \left(\frac{2\pi}{T_z}\right)^4 \omega^{-4}\right) \\ T_z = 0.7105 T_p \end{cases} \quad (15)$$

where T_z is the zero-crossing period.

(3) Ochi-Hubble spectrum [41]:

$$S_\omega(\omega) = \frac{1}{4} \sum_{i=1}^2 \frac{(\lambda_i + \frac{1}{4})^{\lambda_i}}{\Gamma(\lambda_i)} \left(\frac{2\pi}{T_{p,i}}\right)^{4\lambda_i} \frac{H_{s,i}^2}{\omega^{4\lambda_i+1}} \exp\left(-\frac{(\lambda_i + \frac{1}{4})}{\omega^4} \left(\frac{2\pi}{T_{p,i}}\right)^4\right) \quad (16)$$

where $H_{s,i}$, $T_{p,i}$, and λ_i ($i = 1$ or 2) are the significant wave height, peak period, and shape parameter of the low/high frequency section, respectively. Herein, these six parameters can be separately given by a function of the significant wave height H_s ($H_s = \sqrt{H_{s,1}^2 + H_{s,2}^2}$) for the Ochi-Hubble spectrum.

According to the above three wave spectra, eight sea states, i.e., SS1–SS8, can be defined in Table 2. Among them, SS1–SS5 are set as the standard JONSWAP spectra with different significant wave heights H_s and peak periods T_p in order to study the MPPT performance for the same wave-spectrum type but different H_s or T_p . Meanwhile, SS6–SS8 are defined as the JONSWAP spectrum, P-M spectrum, and Ochi-Hubble spectrum with the same H_s^2 , respectively, for the sake of investigation into the MPPT performance of different wave-spectrum types. Moreover, the other investigated characteristic periods T_c of each sea state are also shown in Table 2. The selection criteria of an investigated T_c is based on whether it is common and easily available from the wave spectra of irregular wave environments, wherein the energy period T_e , the mean period T_m , and the zero-crossing period T_z can all be conveniently obtained via spectral moments. The definition for a n -th spectral moment m_n is

$$m_n = \int_0^\infty \omega^n S(\omega) d\omega \quad (17)$$

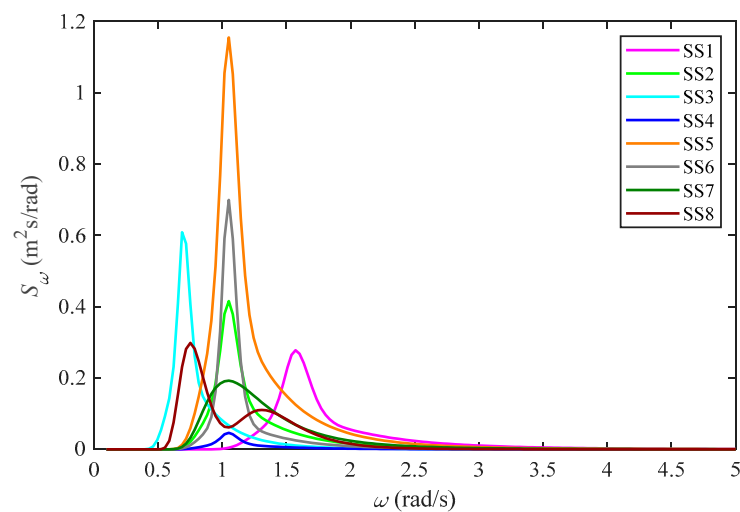
Thereby T_e , T_m , and T_z can be given by

$$\begin{cases} T_e = 2\pi m_{-1}/m_0 \\ T_m = 2\pi m_0/m_1 \\ T_z = 2\pi\sqrt{m_0/m_2} \end{cases} \quad (18)$$

In addition, the wave spectrum density functions of the eight sea states are all displayed in Figure 8.

Table 2. Parameter settings for the simulated sea states.

Sea State	Wave-Spectrum Type	H_s or $H_{s,1}/H_{s,2}$ (m)	T_p or $T_{p,1}/T_{p,2}$ (s)	λ_1/λ_2	T_e (s)	T_m (s)	T_z (s)
SS1	Standard JONSWAP spectrum	1.5	4	/	3.61	3.35	3.15
SS2	Standard JONSWAP spectrum	1.5	6	/	5.42	5.01	4.69
SS3	Standard JONSWAP spectrum	1.5	9	/	8.13	7.51	7.01
SS4	Standard JONSWAP spectrum	0.5	6	/	5.42	5.01	4.69
SS5	Standard JONSWAP spectrum	2.5	6	/	5.42	5.01	4.69
SS6	JONSWAP spectrum ($\gamma = 10$)	1.5	6	/	5.66	5.38	5.14
SS7	JONSWAP spectrum ($\gamma = 1$), i.e., P-M spectrum	1.5	6	/	5.14	4.64	4.29
SS8	Ochi-Hubble spectrum	1.12/1.03	8.36/4.76	3.43/2.04	6.35	5.64	5.29

**Figure 8.** Wave spectrum density functions of eight sea states.

4.3. MPPT

4.3.1. MPPT Implementation Methods

In order to examine the effectiveness of the three implementation methods, the NIP-WEC time-domain response in the regular wave with a wave period of 6 s and a wave height of 0.5 m was simulated. All the parameters are set for the optimal phase and amplitude. For M1, $X = 1$ m, $R_{PTO} = 49,000$ Nms. With regard to M2, $K_{PTO} = -1.055 \times 10^6$ Nm, and $R_{PTO} = 79,000$ Nms. In terms of M3, $K_{PTO} = -1.055 \times 10^6$ Nm, and $R_{PTO} = 43,000$ Nms. Moreover, the calculation formulas for the instantaneous input power P_{IN} , absorbed power P_{PTO} , PTO active power P_R , and PTO reactive power P_K are

$$\begin{cases} P_{IN} = M_E \dot{\theta} \\ P_{PTO} = -M_{PTO} \dot{\theta} \\ P_R = R_{PTO} \dot{\theta}^2 \\ P_K = K_{PTO} \theta \dot{\theta} \text{ or } P_K = K_{PTO} \sin \theta \dot{\theta} \end{cases} \quad (19)$$

According to M1, X_{\max} , $R_{PTO\max}$, the maximum time-averaged absorbed power $\bar{P}_{PTO\max}$, and the maximum capture widths CW_{\max} corresponding to the diverse NIP-WEC MPPs were obtained by a series of time-domain simulations in the regular waves of different wave periods and wave heights. Herein, CW_{\max} is computed by

$$CW_{\max} = \bar{P}_{PTO\max} / J_r = \overline{R_{PTO\max} \dot{\theta}^2} / J_r \quad (20)$$

where J_r signifies the input wave power per unit width for a certain regular wave.

4.3.2. MLTB MPPT

The resonant states where the NIPWEC natural period is consistent with the four T_c , i.e., T_p , T_e , T_m , and T_z , were comprehensively investigated for power assessments in terms of irregular waves. Herein, three prerequisites are set uniformly. First, the simulation duration of each case is set as 1000 s. Second, the optimal, fixed PTO damping R_{PTO_OFD} against a resonant state is searched ergodically from 0 to 2×10^5 Nms (with an interval of 1×10^4 Nms) in order to find the maximum time-averaged absorbed power \bar{P}_{PTO_OFD} under the mode of fixed PTO damping. Third, for the sake of the sensitivity study, the resonant states of the NIPWEC natural period are equal to $0.95\text{--}1.05 T_c$ (with an interval of $0.025 T_c$); these were researched. In addition, the sum δ_{var} of the absolute values of the maximum positive/negative relative deviations was chosen as a unified sensitivity indicator for a certain variable var , e.g., \bar{P}_{PTO_OFD} or R_{PTO_OFD} . A larger δ_{var} means that var is more sensitive to a certain T_c .

In order to study the time-averaged absorbed power and parameter sensitivity of different PTO damping tuning algorithms conveniently, the following three prerequisites are set to be consistent. First, the simulation duration of each case is set as 1000 s as well. Second, R_{PTO} is restricted between 20,000 Nms and 200,000 Nms for whichever algorithm is adopted. Thirdly, all studied cases are based on the resonant state, where the natural period of a NIPWEC is identical to the energy period T_e .

The selection criteria of an investigated key parameter for PTO damping tuning simulations are represented by whether the parameter is able to influence the MPPT tracking performance.

In terms of LTB PTO damping tuning, the investigated parameter is the number of single waves k_w . A k_w that is too large could weaken the real-time tracking performance and restrict the ability to obtain globally optimal solutions. However, if k_w is too small, the negative power deviation for tuning processes could be accumulated quickly. This may also limit the capability of optimizing globally. Herein, the cases of $k_w = 1\text{--}10$, i.e., the cases of the variable update duration mainly distributed within 4–90 s, are investigated for the comprehensive power assessments and sensitivity study.

The investigated parameters for a fixed-step P&O algorithm are the PTO-damping step size ΔR_{PTO} and the update duration ΔT . A too large ΔR_{PTO} and a too small ΔT will make the search process unstable. Meanwhile, a too small ΔR_{PTO} and a too large ΔT will result in a reduction in the search speed. Therefore, the cases of $\Delta R_{PTO} = 10,000$ Nms and $\Delta T = 5\text{--}90$ s (with an interval of 5 s), as well as the cases of $\Delta R_{PTO} = 1000\text{--}20,000$ Nms (with an interval of 1000 Nms) and $\Delta T = 10$ s, were simulated in order. Moreover, the initial PTO damping was set to 20,000 Nms.

For an ADM, the step size coefficient a is chosen as an investigated parameter. Like the ΔR_{PTO} for a fixed-step P&O algorithm, a too large a can make the search process unstable, whereas a too small a can result in a reduction in search speed. Therefore, the cases of $a = 500\text{--}10,000$ Nms³ (with an interval of 500 Nms³) were thoroughly researched. Moreover, the ADM sampling time was determined as 0.01 s, whereas its initial PTO damping was also set as 20,000 Nms.

In addition, the overall sensitivity value $|\overline{\Delta_P}|$ is proposed as a unified sensitivity indicator of the three PTO damping tuning algorithms. $|\overline{\Delta_P}|$ can be calculated as

$$|\overline{\Delta_P}| = \frac{1}{m_\Lambda} \sum_{k=1}^{m_\Lambda} \left| \frac{\left(\frac{\bar{P}_{PTO}}{\bar{P}_{PTO_OFD}} \right)_k - \left(\frac{\bar{P}_{PTO}}{\bar{P}_{PTO_OFD}} \right)_{k-1}}{p_k^* - p_{k-1}^*} \right| \quad (21)$$

where m_Λ is the total number of first-order difference quotients, \bar{P}_{PTO} is the time-averaged absorbed power against different PTO damping tuning algorithms, and p^* the normalized value of a parameter. The normalization method of p^* is given by

$$p^* = \frac{p - \min\{p_0, \dots, p_{m_\Lambda}\}}{\max\{p_0, \dots, p_{m_\Lambda}\} - \min\{p_0, \dots, p_{m_\Lambda}\}} \quad (22)$$

A larger $|\overline{\Lambda_p}|$ means that the relative fluctuation of the time-averaged absorbed power is more sensitive to a certain algorithm parameter.

5. Results and Discussion

5.1. Comparison of Three MPPT Implementation Methods

Figure 9 shows the NIPWEC time-domain response against three MPPT implementation methods. The findings are as follows.

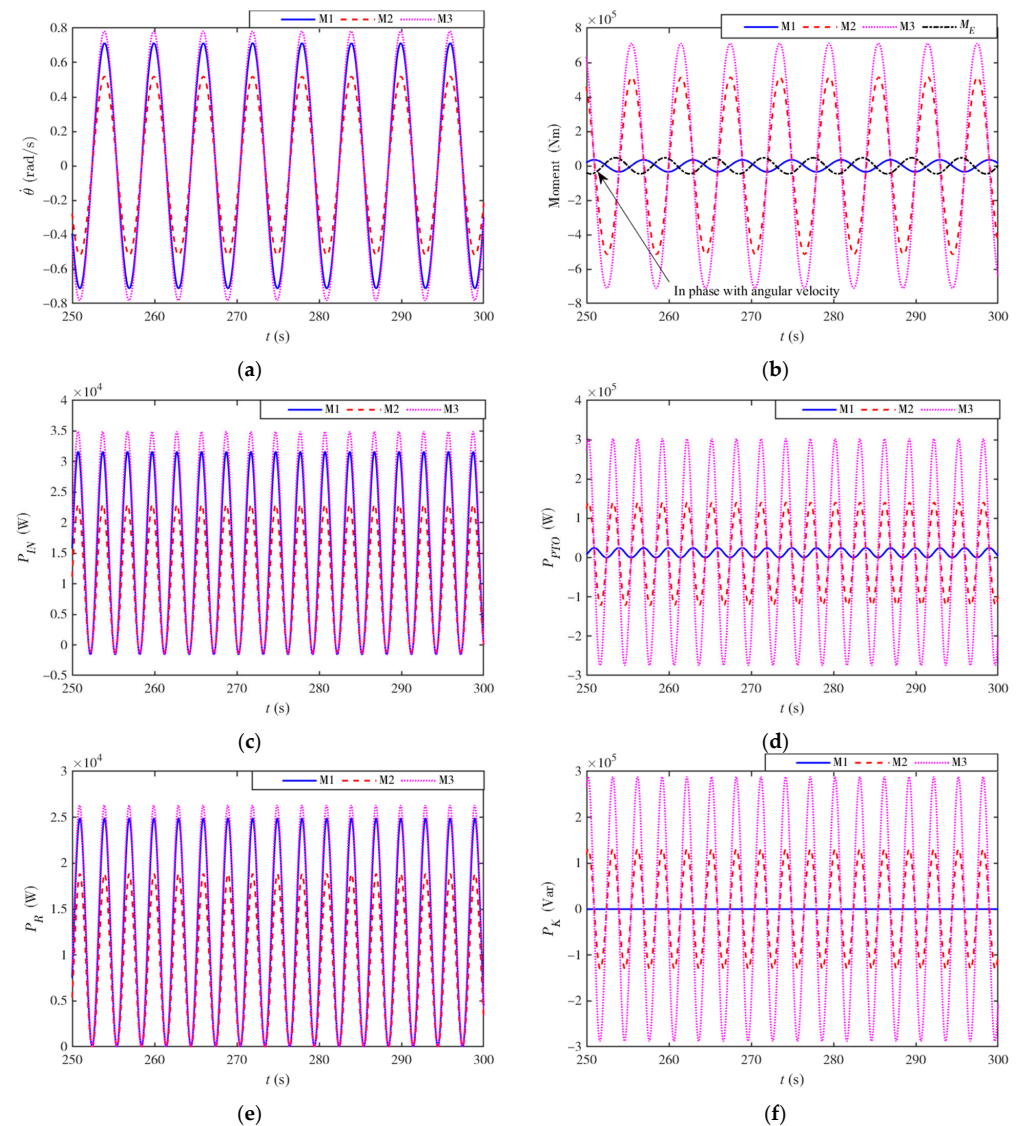


Figure 9. NIPWEC time-domain response against three MPPT implementation methods. (a) Angular velocity: $\dot{\theta}$. (b) PTO moment: M_{PTO} and wave excitation moment: M_E . (c) Input power: P_{IN} . (d) Absorbed power: P_{PTO} . (e) PTO active power: P_R . (f) PTO reactive power: P_K .

(1) All three methods can achieve a basic in-phase situation in terms of the angular velocity $\dot{\theta}$ and the wave excitation moment M_E , which results in the positive value of P_{IN} most of the time (see Figure 9a–c).

(2) Both M1 and M3 can make the NIPWEC operate at the larger $\dot{\theta}$, leading to the higher P_R , when compared to M2.

(3) Both M2 and M3 generate enormous M_{PTO} or P_K , which substantially increases the difficulty of the PTO moment control. The M_{PTO} amplitudes for M2 and M3 can reach approximately 10 times that of M_E , while the P_K amplitudes for them can attain more than five times that of P_{IN} . However, M_{PTO} for M1 has the same magnitude as M_E . Moreover, the P_K for M1 disappears all the time.

In general, M1 can achieve high active power without reactive power generation and the occurrence of an excessive PTO moment. Therefore, the subsequent MPPT research is based on M1.

5.2. MPP Analysis in Regular Waves

The resonance position X_{max} , the optimal PTO damping R_{PTOmax} , the maximum time-averaged absorbed power \bar{P}_{PTOmax} , and the maximum capture widths CW_{max} against different MPPs are listed in Tables 3–6. It should be noted that the wave steepness of some regular waves, e.g., the regular wave of the wave period $T = 3$ s and the wave height $H = 2.5$ m, is greater than 0.1412. According to Schwartz’s theory [42], the aforementioned regular waves do not exist since wave breaking happens. Therefore, the corresponding R_{PTOmax} , \bar{P}_{PTOmax} , and CW_{max} are all set as zero. Three key findings emerge.

Table 3. Resonance position table.

T (s)	3	3.5	4	4.5	5	5.5	6	6.5	7
X_{max} (m)	0.009	0.318	0.524	0.682	0.809	0.913	1	1.071	1.131
T (s)	7.5	8	8.5	9	9.5	10	10.5	11	
X_{max} (m)	1.181	1.225	1.261	1.293	1.32	1.344	1.365	1.383	

Table 4. Optimal PTO damping table. Herein background color is utilized to illustrate the value difference. The deeper red means the larger value, while the deeper blue refers to the smaller one.

R_{PTOmax} (Nms)		H (m)					
		0.5	1	1.5	2	2.5	3
T (s)	3	38,000	41,000	49,000	59,000	0	0
	3.5	51,000	56,000	69,000	83,000	97,000	0
	4	49,000	64,000	83,000	101,000	119,000	135,000
	4.5	46,000	71,000	94,000	115,000	135,000	154,000
	5	46,000	76,000	101,000	124,000	145,000	164,000
	5.5	48,000	79,000	105,000	128,000	149,000	168,000
	6	49,000	80,000	106,000	129,000	150,000	169,000
	6.5	49,000	80,000	105,000	128,000	148,000	167,000
	7	49,000	79,000	104,000	126,000	146,000	164,000
	7.5	48,000	77,000	101,000	122,000	141,000	159,000
	8	47,000	75,000	98,000	119,000	138,000	155,000
	8.5	46,000	73,000	96,000	115,000	134,000	150,000
	9	44,000	71,000	93,000	112,000	129,000	146,000
	9.5	43,000	68,000	89,000	108,000	124,000	140,000
10	41,000	66,000	86,000	104,000	120,000	135,000	
10.5	40,000	64,000	83,000	101,000	116,000	131,000	
11	39,000	62,000	81,000	98,000	113,000	127,000	

Table 5. Maximum time-averaged absorbed power table. Herein background color is utilized to illustrate the value difference. The deeper red means the larger value, while the deeper blue refers to the smaller one.

\bar{P}_{PTOmax} (W)		H (m)					
		0.5	1	1.5	2	2.5	3
T (s)	3	2878	11,360	24,506	41,144	0	0
	3.5	4851	19,065	40,769	67,952	99,427	0
	4	7127	26,706	54,607	88,417	126,927	169,406
	4.5	9713	32,979	63,907	100,355	141,269	185,993
	5	11,644	35,904	66,814	102,619	142,422	185,667
	5.5	12,199	35,260	63,988	96,941	133,371	172,809
	6	11,624	32,420	58,050	87,310	119,572	154,435
	6.5	10,646	28,985	51,416	76,938	105,021	135,329
	7	9489	25,498	45,003	67,158	91,512	117,780
	7.5	8405	22,348	39,281	58,484	79,574	102,310
	8	7248	19,265	33,866	50,431	68,627	88,245
	8.5	6373	16,822	29,487	43,838	59,594	76,572
	9	5545	14,634	25,653	38,141	51,849	66,624
	9.5	4894	12,863	22,511	33,437	45,428	58,348
	10	4305	11,310	19,788	29,390	39,928	51,281
	10.5	3787	9944	17,397	25,836	35,098	45,077
11	3375	8829	15,421	22,880	31,062	39,875	

Table 6. Maximum capture width table. Herein background color is utilized to illustrate the value difference. The deeper red means the larger value, while the deeper blue refers to the smaller one.

CW_{max} (m)		H (m)					
		0.5	1	1.5	2	2.5	3
T (s)	3	3.911	3.859	3.700	3.494	0.000	0.000
	3.5	5.650	5.551	5.276	4.947	4.632	0.000
	4	7.264	6.804	6.184	5.632	5.174	4.796
	4.5	8.799	7.469	6.433	5.682	5.119	4.680
	5	9.494	7.318	6.053	5.229	4.645	4.205
	5.5	9.042	6.534	5.270	4.491	3.954	3.558
	6	7.898	5.507	4.382	3.708	3.250	2.915
	6.5	6.677	4.545	3.583	3.016	2.635	2.358
	7	5.526	3.712	2.912	2.444	2.132	1.905
	7.5	4.568	3.037	2.372	1.987	1.730	1.545
	8	3.693	2.454	1.917	1.606	1.399	1.249
	8.5	3.056	2.017	1.571	1.314	1.143	1.020
	9	2.512	1.657	1.291	1.080	0.939	0.838
	9.5	2.100	1.380	1.073	0.897	0.780	0.696
	10	1.755	1.153	0.896	0.749	0.651	0.581
	10.5	1.470	0.965	0.750	0.627	0.545	0.486
11	1.251	0.818	0.635	0.530	0.460	0.410	

(1) X_{max} is only related to T , but R_{PTOmax} depends on both T and H . As T increases, R_{PTOmax} shows a trend of first increasing and then decreasing. However, as H increases, R_{PTOmax} only shows an increasing trend.

(2) \bar{P}_{PTOmax} is related to both T and H . Moreover, \bar{P}_{PTOmax} appears to have the same variation law as R_{PTOmax} .

(3) CW_{max} is also related to both T and H . Nevertheless, the variation law for CW_{max} is different from that of R_{PTOmax} or \bar{P}_{PTOmax} . As T increases, CW_{max} increases first and then decreases. When H increases, CW_{max} gradually decreases.

Moreover, both \bar{P}_{PTOmax} and CW_{max} were compared with the corresponding solutions from the preliminary frequency-domain calculations in order to verify the correctness of the time-domain simulations (see Figure 10). The results indicate that \bar{P}_{PTOmax} or

CW_{max} is always less than or equal to the frequency-domain solution. When both T and H are small, the frequency-domain solution fits \bar{P}_{PTOmax} or CW_{max} better than other cases. Moreover, the capture widths derived from the time/frequency-domain model are all below the theoretical upper bound. Hence, the time-domain simulation correctness is effectively verified.

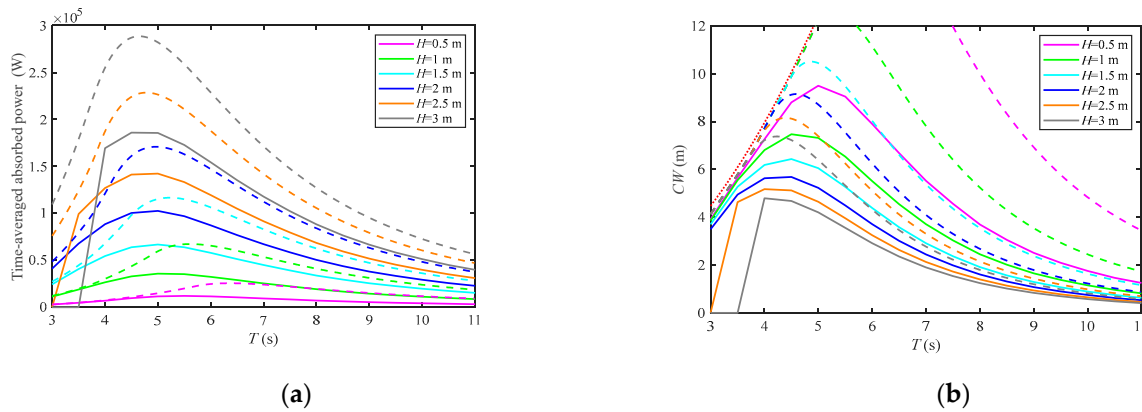


Figure 10. Variations in the time-averaged absorbed power (a) and the capture width CW (b) as the function of T against different H . Note: solid lines: resonance and $R_{PTO} = R_{PTOmax}$; Dashed lines: resonance and $R_{PTO} = \max\{R_{55}(\omega_r), R_{PTO_min}(\omega_r)\}$; Red dotted line: the theoretical upper bound of CW , i.e., λ/π [43]. Herein, $R_{PTO_min}(\omega_r)$ means the minimum PTO damping against $\omega = \omega_r$, which is derived from the upper limitation for the swing angle amplitude. λ is the wavelength.

In order to further explain the variation law of MPPs, the regular waves of $T = 6$ s and $H = 0.5\text{--}3$ m, as well as the ones of $T = 3\text{--}11$ s and $H = 1.5$ m are taken as examples. The time-averaged absorbed power curves against different H or T are displayed in Figure 11. The results show that R_{PTOmax} is usually larger than $R_{55}(\omega_r)$. The difference between R_{PTOmax} and $R_{55}(\omega_r)$ becomes more obvious, along with the increase in H since $R_{55}(\omega_r)$ is independent of H , whereas R_{PTOmax} increases synchronously. In addition, the relationship between R_{PTOmax} and \bar{P}_{PTOmax} presents an approximately quadratic correlation under the circumstance of the same T combined with a different H . Meanwhile, there exists a hysteresis phenomenon in the $R_{PTOmax}\text{--}\bar{P}_{PTOmax}$ relationship, under the circumstance of the same H combined with a different T .

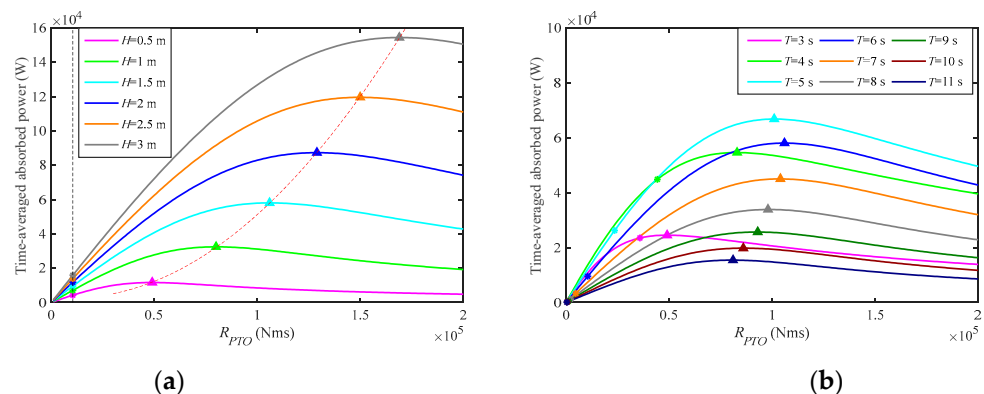


Figure 11. Variations in the time-averaged absorbed power as the function of the linear PTO damping R_{PTO} . (a) $T = 6$ s and $H = 0.5\text{--}3$ m. (b) $T = 3\text{--}11$ s and $H = 1.5$ m. Note: “*”: $R_{PTO} = R_{55}(\omega_r)$; solid triangle points: $R_{PTO} = R_{PTOmax}$.

In summary, the MPPs in regular waves can be effectively gained via time-domain simulations. Moreover, the R_{PTOmax} and $R_{PTOmax}\text{--}\bar{P}_{PTOmax}$ relationship is totally different from the frequency-domain solutions.

5.3. Power Assessments and Sensitivity Study for the LTB Internal-Mass Position Adjustment

The resonant states against different characteristic periods T_c of the eight sea states were simulated. Moreover, the resonant states against 0.95–1.05 T_c were also considered for the sensitivity study. The statistical results of \bar{P}_{PTO_OFD} and R_{PTO_OFD} are listed in Tables 7 and 8, respectively. The largest A_P as well as the corresponding A_R of each sea state is in bold and is underlined. Herein, A_P signifies the arithmetic mean of \bar{P}_{PTO_OFD} , whereas A_R means the arithmetic mean of R_{PTO_OFD} . Moreover, Figure 12 visually displays the energy capture performance of different T_c resonances in the form of a histogram. The maximum \bar{P}_{PTO_OFD} and the minimum \bar{P}_{PTO_OFD} are represented by error bars. The results demonstrate the following three things.

Table 7. Power assessments for resonant states against different characteristic periods T_c . Herein, a sensitivity study is also conducted for 0.95–1.05 T_c . A_P means the arithmetic mean of \bar{P}_{PTO_OFD} , and δ_P is a unified sensitivity indicator for \bar{P}_{PTO_OFD} . The largest A_P of each sea state is in bold and underlined.

Sea State	T_p		T_e		T_m		T_z	
	A_P (w)	δ_P	A_P (w)	δ_P	A_P (w)	δ_P	A_P (w)	δ_P
SS1	<u>15,130</u>	0.072	11,873	0.397	8314	0.416	7296	0.428
SS2	19,366	0.351	<u>23,332</u>	0.162	18,336	0.588	12,778	0.560
SS3	10,320	0.393	<u>13,339</u>	0.096	12,447	0.152	11,274	0.161
SS4	<u>2532</u>	0.238	2078	0.434	1527	0.356	1234	0.327
SS5	44,226	0.279	<u>54,006</u>	0.088	50,535	0.247	41,804	0.376
SS6	23,679	0.394	27,902	0.253	<u>29,488</u>	0.118	25,030	0.585
SS7	14,074	0.257	<u>15,419</u>	0.158	12,609	0.225	10,618	0.298
SS8	8248	0.285	8906	0.393	8642	0.109	<u>9214</u>	0.125

Table 8. Analysis of the optimal, fixed PTO damping R_{PTO_OFD} for the resonant states against different characteristic periods T_c . Herein, a sensitivity study was also conducted for 0.95–1.05 T_c . A_R means the arithmetic mean of R_{PTO_OFD} , and δ_R is a unified sensitivity indicator for R_{PTO_OFD} . The A_R against the largest A_P of each sea state is in bold and underlined.

Sea State	T_p		T_e		T_m		T_z	
	A_R (Nms)	δ_R	A_R (Nms)	δ_R	A_R (Nms)	δ_R	A_R (Nms)	δ_R
SS1	<u>76,000</u>	0.263	104,000	0.673	170,000	0.412	188,000	0.213
SS2	82,000	0.366	<u>52,000</u>	0.577	30,000	0.667	68,000	1.765
SS3	64,000	0.469	<u>42,000</u>	0.476	36,000	0.278	32,000	0.625
SS4	<u>34,000</u>	0.588	62,000	0.806	102,000	0.490	132,000	0.379
SS5	122,000	0.246	<u>94,000</u>	0.319	74,000	0.270	66,000	0.455
SS6	86,000	0.349	70,000	0.286	<u>52,000</u>	0.769	32,000	0.938
SS7	72,000	0.417	<u>48,000</u>	0.625	74,000	0.811	100,000	0.500
SS8	70,000	0.286	96,000	1.354	142,000	0.634	<u>110,000</u>	0.364

(1) Although there is a certain possibility for all T_c resonances to obtain the largest A_P , it is better to keep resonant with T_e because T_e resonance can lead 50% of sea states to achieve the largest A_P , as well as allowing other sea states to obtain a submaximal A_P .

(2) When the largest A_P is achieved, the unified sensitivity indicator δ_P for \bar{P}_{PTO_OFD} is relatively low. This means that \bar{P}_{PTO_OFD} is not sensitive to the fine tuning of T_c when \bar{P}_{PTO_OFD} appears around the largest A_P . Moreover, T_e resonance owns the minimum or subminimum δ_P in six out of eight sea states. Hence, T_e resonance is not sensitive to parameter changes in most sea states.

(3) Despite being in the same sea state, A_R against different T_c is quite different, and the change law of A_R along with the variations in T_c is elusive. Moreover, in contrast

to \bar{P}_{PTO_OFD} , R_{PTO_OFD} is still sensitive to the fine tuning of T_c when \bar{P}_{PTO_OFD} appears around the largest A_p .

In summary, T_e resonance is preferable in terms of power assessments when compared to other T_c resonances. Moreover, the performance reliability of the T_e resonance is high since its parameter sensitivity is low in most sea states. Hence, the subsequent simulations for three PTO damping tuning algorithms are all based on the T_e resonance.

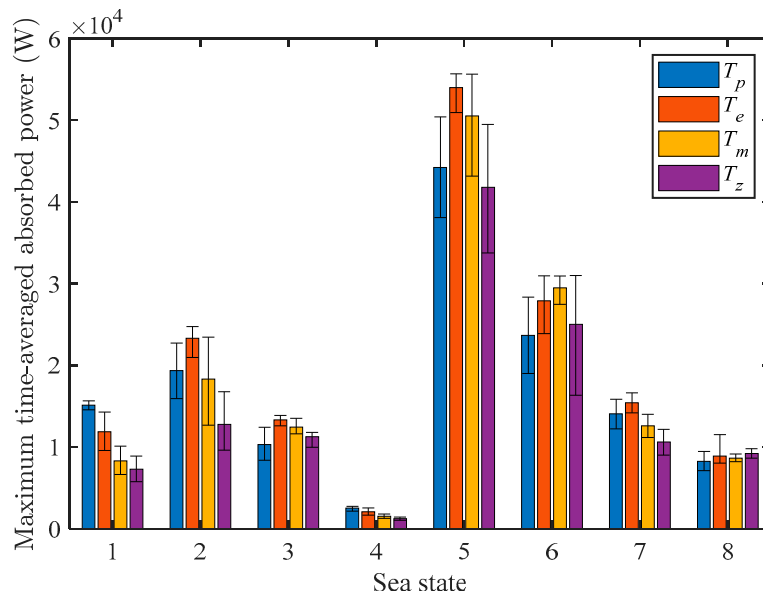


Figure 12. Histogram about the maximum time-averaged absorbed power \bar{P}_{PTO_OFD} at different resonant states against different characteristic periods, T_c . Herein, the upper and lower bounds are displayed in the form of error bars.

5.4. Power Assessments and Sensitivity Study for the LTB PTO Damping Tuning

Power assessments for the three PTO damping tuning algorithms, i.e., the fixed-step P&O algorithm and the ADM and LTB PTO damping tuning algorithms, are listed in Tables 9–11. The upper bound of the maximum or mean \bar{P}_{PTO} of three algorithms in each sea state is in bold and underlined. The results indicate the following three facts.

Table 9. Power assessments of the fixed-step P&O algorithm. Herein, a sensitivity study was also conducted for $\Delta R_{PTO} = 10,000$ Nms with $\Delta T = 5\text{--}90$ s, as well as $\Delta T = 10$ s, with $\Delta R_{PTO} = 1000\text{--}20,000$ Nms. The upper bound of the maximum or mean \bar{P}_{PTO} of three algorithms in each sea state is in bold and underlined.

Sea State	$\Delta R_{PTO} = 10,000$ Nms				$\Delta T = 10$ s				Overall Assessment		
	<u>Max.</u> P_{PTO} (W)	<u>Min.</u> P_{PTO} (W)	<u>Mean</u> P_{PTO} (W)	$ \Delta P $	<u>Max.</u> P_{PTO} (W)	<u>Min.</u> P_{PTO} (W)	<u>Mean</u> P_{PTO} (W)	$ \Delta P $	<u>Max.</u> P_{PTO} (W)	<u>Min.</u> P_{PTO} (W)	<u>Mean</u> P_{PTO} (W)
SS1	11,391	7938	10,093	1.394	11,567	7706	10,565	0.391	11,567	7706	10,341
SS2	23,685	18,331	20,867	0.877	23,680	16,367	20,363	1.068	<u>23,685</u>	16,367	<u>20,602</u>
SS3	12,476	10,264	11,733	0.787	12,759	9761	11,322	0.518	<u>12,759</u>	9761	<u>11,517</u>
SS4	2050	1806	1941	0.653	2051	1834	1976	0.425	2051	1806	1959
SS5	50,986	29,542	40,615	1.016	52,211	23,873	44,061	1.105	52,211	23,873	42,429
SS6	26,525	18,146	21,973	1.446	25,688	16,831	23,159	0.935	26,525	16,831	22,598
SS7	16,494	13,976	15,239	0.771	15,756	13,609	14,719	0.5	<u>16,494</u>	13,609	14,965
SS8	7449	5964	6833	0.856	7500	6245	7198	0.282	7500	5964	7025

Table 10. Power assessments of the ADM. Herein, a sensitivity study was also conducted for $a = 500\text{--}10,000 \text{ Nms}^3$. The upper bound of the maximum or mean \bar{P}_{PTO} of three algorithms in each sea state is in bold and underlined.

Sea State	Overall Assessment			
	Maximum \bar{P}_{PTO} (W)	Minimum \bar{P}_{PTO} (W)	Mean \bar{P}_{PTO} (W)	$ \Lambda_P $
SS1	<u>11,923</u>	9035	11,075	0.824
SS2	<u>22,726</u>	14,662	16,270	1.672
SS3	9923	7519	8002	0.948
SS4	1971	1593	1693	1.159
SS5	52,908	41,723	44,649	1.321
SS6	25,141	17,426	18,953	1.358
SS7	14,884	12,581	13,138	0.686
SS8	<u>8144</u>	7823	<u>7957</u>	0.196

Table 11. Power assessments of the LTB PTO damping tuning. Herein, a sensitivity study was also conducted for $k_w = 1\text{--}10$. The upper bound of the maximum or mean \bar{P}_{PTO} of three algorithms in each sea state is in bold and underlined.

Sea State	Overall Assessment			
	Maximum \bar{P}_{PTO} (W)	Minimum \bar{P}_{PTO} (W)	Mean \bar{P}_{PTO} (W)	$ \Lambda_P $
SS1	11,790	11,446	<u>11,631</u>	0.052
SS2	21,048	19,776	20,513	0.107
SS3	11,176	10,445	10,770	0.063
SS4	<u>2091</u>	2023	<u>2055</u>	0.042
SS5	<u>53,329</u>	50,272	<u>51,588</u>	0.130
SS6	<u>27,871</u>	26,952	<u>27,387</u>	0.098
SS7	15,611	14,642	<u>15,017</u>	0.149
SS8	8020	7705	7902	0.102

(1) In terms of the mean \bar{P}_{PTO} against the different parameters, LTB PTO damping tuning can obtain the maximum mean value in five out of eight sea states. Moreover, it can also achieve submaximum mean values in the other sea states. However, the fixed-step P&O algorithm can only get the maximum mean value in SS2 or SS3. Moreover, ADM has the best tracking performance for the SS8 of an Ochi-Hubble spectrum.

(2) For the maximum value of the time-averaged absorbed power against the different parameters, the obtaining probability of the three algorithms are not significantly different.

(3) With regard to $|\Lambda_P|$, both the $|\Lambda_P|$ of the fixed-step P&O algorithm and the $|\Lambda_P|$ of the ADM are much larger than that of the LTB PTO damping tuning. Therefore, the former two algorithms are more sensitive to parameter changes than the LTB PTO damping tuning. Moreover, the fixed-step P&O algorithm is more sensitive to ΔT than to ΔR_{PTO} .

Figure 13 visually displays the \bar{P}_{PTO} of the three algorithms in the form of a histogram, wherein the maximum \bar{P}_{PTO} and the minimum \bar{P}_{PTO} are represented by error bars. From Figure 13, it can be seen that the bar length, i.e., the mean \bar{P}_{PTO} , of the LTB PTO damping tuning is generally higher, and its error bar is the narrowest. Although the fixed-step P&O algorithm and ADM can obtain the maximum average absorbed power under certain sea states through parameter tuning, such as the fixed-step P&O algorithm in SS2, SS3, or SS7 (with the optimal $\{\Delta R_{PTO}, \Delta T\} = \{5000 \text{ Nms}, 10 \text{ s}\}$, $\{8000 \text{ Nms}, 10 \text{ s}\}$ or $\{10,000 \text{ Nms}, 80 \text{ s}\}$, respectively), and the ADM in SS1 or SS8 (with the optimal $a = 1500 \text{ Nms}^3$ or 4000 Nms^3 , respectively), the mean \bar{P}_{PTO} of them is generally low and owns a wider error bar.

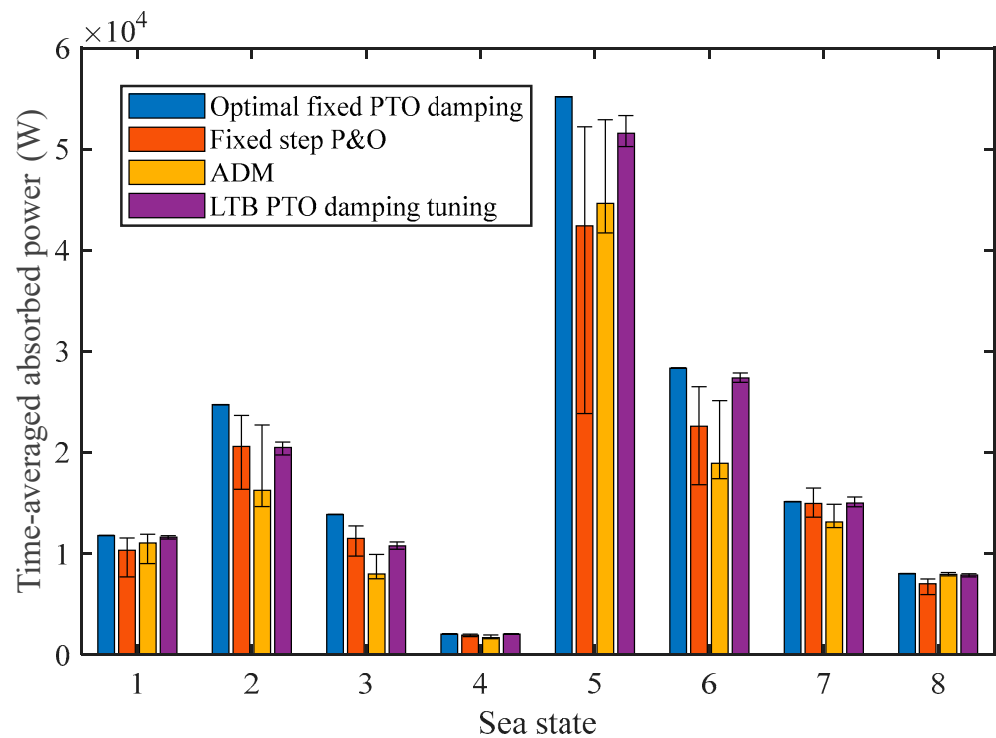


Figure 13. Time-averaged absorbed power histogram against different PTO damping tuning algorithms. Herein, \bar{P}_{PTO_OFD} against optimal, fixed PTO damping R_{PTO_OFD} is also illustrated as a reference. Moreover, the upper and lower bounds are displayed in the form of error bars.

Furthermore, we take SS2, SS5, SS6, and SS7 as examples. The variations in \bar{P}_{PTO} as a function of the algorithm parameters against the above sea states are displayed in Figure 14 for the sake of the visual indication of the specific impact of parameter changes on algorithm performance. It can be seen that \bar{P}_{PTO} fluctuates at a wide range with no obvious change pattern when the ΔT or ΔR_{PTO} alters equidistantly. When a changes in an equal interval, the fluctuation range of the average absorption power of the ADM is smaller than that of the fixed-step P&O algorithm. However, there exist several sudden increases at certain values of a . When k_w increases one by one, the variations in \bar{P}_{PTO} against the LTB PTO damping tuning is the smoothest without significant fluctuations.

In summary, the LTB PTO damping tuning is the least sensitive to parameter changes and has a high average absorbed power value. The overall reliability of this algorithm is high. Although the fixed-step P&O method and admittance differentiation method can search for larger power points against some specific parameters and sea states, the optimal parameters corresponding to the above power points have significant differences in different sea states, which makes it difficult to determine the universal optimal parameters. Moreover, the high sensitivity to parameter changes is another limitation.

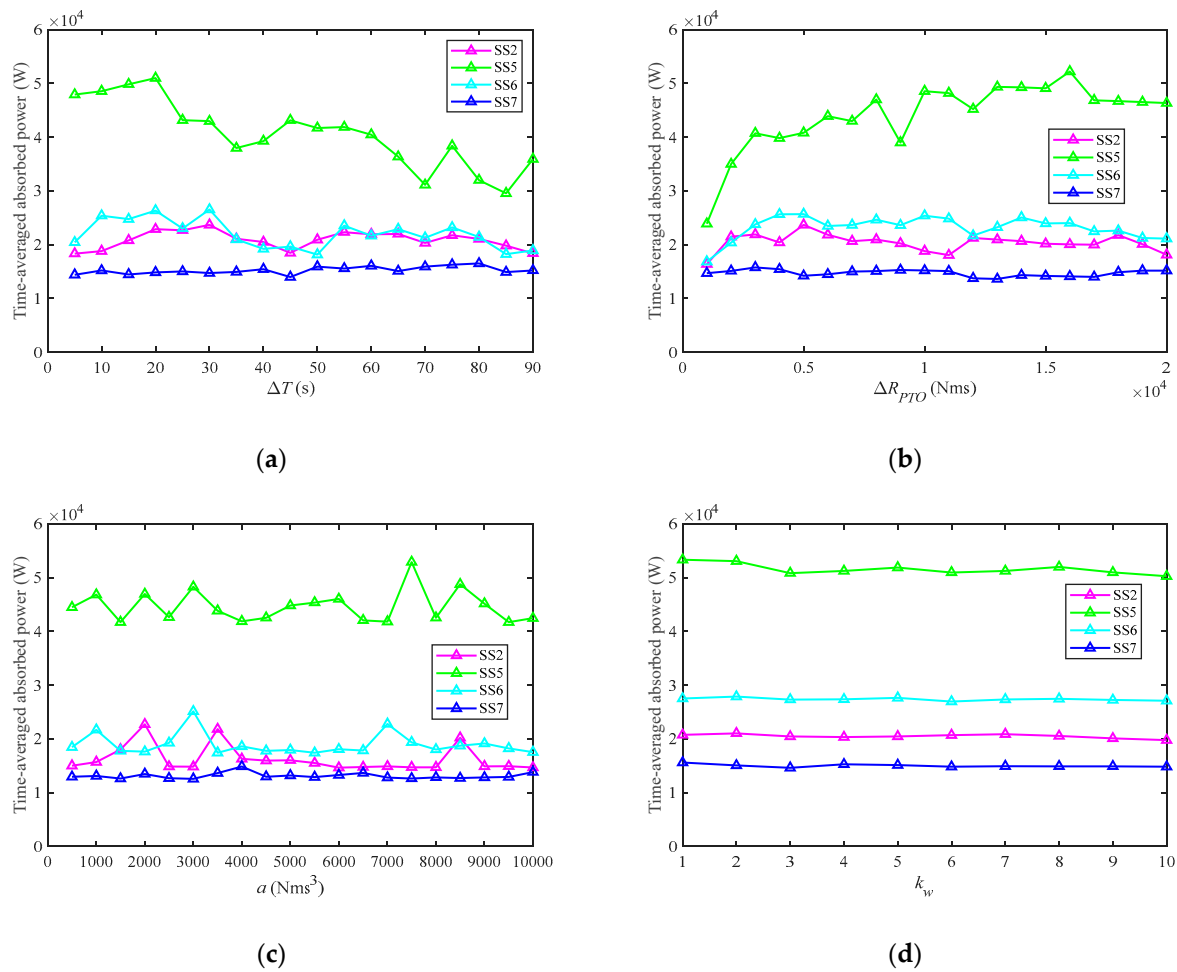


Figure 14. Variations in \bar{P}_{PTO} as a function of the parameters of different PTO damping tuning algorithms in four sea states. (a) ΔT of the fixed-step P&O algorithm. (b) ΔR_{PTO} of the fixed-step P&O algorithm. (c) a of the ADM. (d) k_w of the LTB PTO damping tuning.

6. Conclusions

This paper attempts to find a suitable MPPT technology for the optimized operation of a NIPWEC. First, a unique MPPT implementation method, i.e., adjusting the internal-mass position to achieve “optimal phase” and tuning the linear PTO damping to achieve “optimal amplitude”, was proposed. Then, MPPs in regular waves were discussed, and two lookup tables, i.e., a 1D resonance position table and a 2D optimal PTO damping table, were determined. Afterwards, an MLTB MPPT algorithm was put forward for the NIPWEC real-time operation in irregular waves, according to the aforementioned two lookup tables. MLTB MPPT consists of two core parts, i.e., the LTB internal-mass position adjustment and the LTB PTO damping tuning. Finally, the power assessments and sensitivity study for the LTB internal-mass position adjustment and the LTB PTO damping tuning were respectively conducted for eight simulated irregular-wave sea states of diverse wave spectra. The findings are as follows.

(1) It is preferable to choose M1, i.e., simultaneously adjusting the internal mass position and PTO damping, to realize MPPT. First, M1 has the same active power generation performance as the PTO impedance adjustment, with consideration given to the nonlinear effect of the hydrostatic restoring moment. Second, M1 does not generate excessive reactive power and PTO moment.

(2) For the LTB internal-mass position adjustment in irregular waves, energy period resonance possesses the highest possibility to obtain the maximum mean time-averaged absorbed power when compared with other characteristic period resonances. Moreover,

the energy period resonance has high reliability since its parameter sensitivity is low in most sea states.

(3) When compared to the fixed-step P&O algorithm and a typical variable-step P&O algorithm, i.e., ADM, LTB PTO damping tuning is the most robust to parameter changes and has the highest mean time-averaged absorbed power in the majority of sea states.

In the future, the tracking performance of MLTB MPPT in changing sea states will be studied in-depth in order to further validate its applicability.

Author Contributions: Conceptualization, X.Y. and Q.C.; methodology, X.Y.; software, X.Y. and D.G.; validation, J.Z., F.M. and D.G.; formal analysis, X.Y.; investigation, D.G.; data curation, J.L.; writing—original draft preparation, X.Y.; writing—review and editing, D.G.; visualization, X.Y.; supervision, Q.C. and J.L.; funding acquisition, J.Z. and F.M. All authors have read and agreed to the published version of the manuscript.

Funding: This research was funded by the National Natural Science Foundation of China (Grant No. 52179088) and the Science & Technology Project of Enterprise (Grant No. ZKY2023-HCDK-02-01).

Data Availability Statement: Not applicable.

Conflicts of Interest: The authors declare no conflict of interest.

References

- Guo, B.; Ringwood, J.V. A Review of Wave Energy Technology from a Research and Commercial Perspective. *IET Renew. Power Gener.* **2021**, *15*, 3065–3090. [CrossRef]
- Huckerby, J.; Jeffrey, H.; de Andres, A.; Finlay, L. *An International Vision for Ocean Energy*; OES: Lisbon, Portugal, 2017.
- IEA Electricity Consumption—Electricity Information: Overview. Available online: <https://www.iea.org/reports/electricity-information-overview/electricity-consumption#abstract> (accessed on 31 May 2023).
- López, I.; Andreu, J.; Ceballos, S.; Martínez De Alegría, I.; Kortabarria, I. Review of Wave Energy Technologies and the Necessary Power-Equipment. *Renew. Sustain. Energy Rev.* **2013**, *27*, 413–434. [CrossRef]
- Sheng, W. Wave Energy Conversion and Hydrodynamics Modelling Technologies: A Review. *Renew. Sustain. Energy Rev.* **2019**, *109*, 482–498. [CrossRef]
- Falnes, J. *Ocean Waves and Oscillating Systems: Linear Interaction Including Wave Energy Extraction*; Cambridge University Press: Cambridge, MA, USA, 2002; ISBN 0511030932.
- Wu, J.; Yao, Y.; Zhou, L.; Göteman, M. Real-Time Latching Control Strategies for the Solo Duck Wave Energy Converter in Irregular Waves. *Appl. Energy* **2018**, *222*, 717–728. [CrossRef]
- Garcia-Rosa, P.B.; Fosso, O.B.; Molinas, M. Switching Sequences for Non-Predictive Declutching Control of Wave Energy Converters. *IFAC-PapersOnLine* **2020**, *53*, 12295–12300. [CrossRef]
- Costa, P.R.; Garcia-Rosa, P.B.; Estefen, S.F. Phase Control Strategy for a Wave Energy Hyperbaric Converter. *Ocean Eng.* **2010**, *37*, 1483–1490. [CrossRef]
- Qiu, S.; Ye, J.; Wang, D.; Liang, F. Experimental Study on a Pendulum Wave Energy Converter. *China Ocean Eng.* **2013**, *27*, 359–368. [CrossRef]
- Marei, M.I.; Mokhtar, M.; El-Sattar, A.A. MPPT Strategy Based on Speed Control for AWS-Based Wave Energy Conversion System. *Renew. Energy* **2015**, *83*, 305–317. [CrossRef]
- Chen, Q.; Shang, X.; Huang, X.; Tan, T.; Chen, X.; Xu, Z. Resonant Wave Energy Power Take-off System Based on Hydraulic Transmission. *Autom. Electr. Power Syst.* **2016**, *40*, 115–120.
- Wu, J.; Yao, Y.; Li, W.; Zhou, L.; Göteman, M. Optimizing the Performance of Solo Duck Wave Energy Converter in Tide. *Energies* **2017**, *10*, 289. [CrossRef]
- Cai, Y.; Huo, Y.; Shi, X.; Liu, Y. Numerical and Experimental Research on a Resonance-Based Wave Energy Converter. *Energy Convers. Manag.* **2022**, *269*, 116152. [CrossRef]
- Cai, Y.; Shi, X.; Huo, Y.; Liu, Y. Experimental Study on a Pitching Wave Energy Converter with Adjustable Natural Period. *Ocean Eng.* **2022**, *261*, 112128. [CrossRef]
- Zheng, Y.; Chen, Q.; Yue, X.; Geng, D.; Niu, Y.; Gu, X. Active-Resonance Technology for Wave Energy Utilization: An Efficient Offshore Distributed Renewable Power Generation Alternative. *Energy Convers. Manag.* **2023**, *292*, 117359. [CrossRef]
- Tom, N.; Lawson, M.; Yu, Y.-H.; Wright, A. Spectral Modeling of an Oscillating Surge Wave Energy Converter with Control Surfaces. *Appl. Ocean Res.* **2016**, *56*, 143–156. [CrossRef]
- Qasim, M.A.; Alwan, N.T.; PraveenKumar, S.; Velkin, V.I.; Agyekum, E.B. A New Maximum Power Point Tracking Technique for Thermoelectric Generator Modules. *Inventions* **2021**, *6*, 88. [CrossRef]
- Amon, E.A.; Schacher, A.A.; Brekken, T.K.A. A Novel Maximum Power Point Tracking Algorithm for Ocean Wave Energy Devices. In Proceedings of the 2009 IEEE Energy Conversion Congress and Exposition, ECCE 2009, San Jose, CA, USA, 20–24 September 2009; pp. 2635–2641.

20. Mendes, R.; Calado, M.D.R.; Mariano, S. Maximum Power Point Tracking for a Point Absorber Device with a Tubular Linear Switched Reluctance Generator. *Energies* **2018**, *11*, 2192. [[CrossRef](#)]
21. Artal-Sevil, J.S.; Martínez-López, D.; Guillén-Asensio, A.; Domínguez-Navarro, J.A. Wave Energy Converter Model Based on a Decentralized Hybrid Energy Storage System with MPPT Control Algorithm. In Proceedings of the 2020 Fifteenth International Conference on Ecological Vehicles and Renewable Energies (EVER), Monte-Carlo, Monaco, 10–12 September 2020; pp. 1–11.
22. Ugaz Peña, J.C.; Medina Rodríguez, C.L.; Guarniz Avalos, G.O. Study of a New Wave Energy Converter with Perturb and Observe Maximum Power Point Tracking Method. *Sustainability* **2023**, *15*, 447. [[CrossRef](#)]
23. Yang, J. *Research on Key Technologies of Horizontal Pendulum Wave Energy Converter*; Zhejiang University: Hangzhou, China, 2018.
24. Zhou, Y. *Research on the Power Control Technology of Floating Pendulum Wave Energy Converter*; Zhejiang University: Hangzhou, China, 2019.
25. Xu, J.; Yang, Y.; Hu, Y.; Xu, T.; Zhan, Y. MPPT Control of Hydraulic Power Take-off for Wave Energy Converter on Artificial Breakwater. *J. Mar. Sci. Eng.* **2020**, *8*, 304. [[CrossRef](#)]
26. Mishra, S.; Purwar, S.; Kishor, N. Maximizing Output Power in Oscillating Water Column Wave Power Plants: An Optimization Based MPPT Algorithm. *Technologies* **2018**, *6*, 15. [[CrossRef](#)]
27. Yue, X.; Geng, D.; Chen, Q.; Zheng, Y.; Gao, G.; Xu, L. 2-D Lookup Table Based MPPT: Another Choice of Improving the Generating Capacity of a Wave Power System. *Renew. Energy* **2021**, *179*, 625–640. [[CrossRef](#)]
28. Zhao, A.; Wu, W.; Sun, Z.; Zhu, L.; Lu, K.; Chung, H.; Blaabjerg, F. A Flower Pollination Method Based Global Maximum Power Point Tracking Strategy for Point-Absorbing Type Wave Energy Converters. *Energies* **2019**, *12*, 1343. [[CrossRef](#)]
29. M'zoughi, F.; Garrido, I.; Garrido, A.J.; De La Sen, M. Rotational Speed Control Using ANN-Based MPPT for OWC Based on Surface Elevation Measurements. *Appl. Sci.* **2020**, *10*, 8975. [[CrossRef](#)]
30. Agyekum, E.B.; PraveenKumar, S.; Eliseev, A.; Velkin, V.I. Design and Construction of a Novel Simple and Low-Cost Test Bench Point-Absorber Wave Energy Converter Emulator System. *Inventions* **2021**, *6*, 20. [[CrossRef](#)]
31. Yao, G.; Luo, Z.; Lu, Z.; Wang, M.; Shang, J.; Guerrerob, J.M. Unlocking the Potential of Wave Energy Conversion: A Comprehensive Evaluation of Advanced Maximum Power Point Tracking Techniques and Hybrid Strategies for Sustainable Energy Harvesting. *Renew. Sustain. Energy Rev.* **2023**, *185*, 113599. [[CrossRef](#)]
32. Dong, F.; Pan, S.; Gong, J.; Cai, Y. Maximum Power Point Tracking Control Strategy Based on Frequency and Amplitude Control for the Wave Energy Conversion System. *Renew. Energy* **2023**, *215*, 118973. [[CrossRef](#)]
33. Ouyang, Z.; Zheng, Y.; Yue, X.; Chen, Q. Wave-to-Wire Dynamic Modeling and Time-Domain Characteristic Analysis for the Novel Inverse-Pendulum Wave Energy Converter. *J. Ocean Technol.* **2023**, *42*, 94–104. [[CrossRef](#)]
34. Peña-Sanchez, Y.; Windt, C.; Davidson, J.; Ringwood, J.V. A Critical Comparison of Excitation Force Estimators for Wave-Energy Devices. *IEEE Trans. Control Syst. Technol.* **2020**, *28*, 2263–2275. [[CrossRef](#)]
35. Hillis, A.J.; Brask, A.; Whitlam, C. Real-Time Wave Excitation Force Estimation for an Experimental Multi-DOF WEC. *Ocean Eng.* **2020**, *213*, 107788. [[CrossRef](#)]
36. Lobeto, H.; Menendez, M.; Losada, I.J. Future Behavior of Wind Wave Extremes Due to Climate Change. *Sci. Rep.* **2021**, *11*, 7869. [[CrossRef](#)]
37. Cummins, W.E. The Impulse Response Function and Ship Motion. *Schiffstechnik* **1962**, *9*, 101–109.
38. Sheng, W.; Alcorn, R.; Lewis, A. A New Method for Radiation Forces for Floating Platforms in Waves. *Ocean Eng.* **2015**, *105*, 43–53. [[CrossRef](#)]
39. Xuhui, Y.; Qijuan, C.; Zenghui, W.; Dazhou, G.; Donglin, Y.; Wen, J.; Weiyu, W. A Novel Nonlinear State Space Model for the Hydraulic Power Take-off of a Wave Energy Converter. *Energy* **2019**, *180*, 465–479. [[CrossRef](#)]
40. Molin, B. *Hydrodynamique des Structures Offshore*; Editions Technip: Paris, France, 2002; ISBN 2710808153.
41. Golpira, A.; Panahi, R.; Shafieefar, M. Developing Families of Ochi-Hubble Spectra for the Northern Parts of the Gulf of Oman. *Ocean Eng.* **2019**, *178*, 345–356. [[CrossRef](#)]
42. Schwartz, L.W. Computer Extension and Analytic Continuation of Stokes' Expansion for Gravity Waves. *J. Fluid Mech.* **1974**, *62*, 553–578. [[CrossRef](#)]
43. Babarit, A. A Database of Capture Width Ratio of Wave Energy Converters. *Renew. Energy* **2015**, *80*, 610–628. [[CrossRef](#)]

Disclaimer/Publisher's Note: The statements, opinions and data contained in all publications are solely those of the individual author(s) and contributor(s) and not of MDPI and/or the editor(s). MDPI and/or the editor(s) disclaim responsibility for any injury to people or property resulting from any ideas, methods, instructions or products referred to in the content.